Systematic Errors in Black Hole Mass Measurement Using Reverberation Mapping

A Senior Honors Thesis

Presented in Partial Fulfillment of the Requirements for graduation *with research distinction* in Astronomy in the undergraduate colleges of The Ohio State University

by

Megan L. Comins

The Ohio State University
June 2008

Project Advisor: Professor Bradley M. Peterson, Department of Astronomy

1 Abstract

Active galactic nuclei (AGNs) are extremely energetic central regions of galaxies whose brightness cannot be attributed to stars alone. A typical AGN emits at least the same amount of energy that is emitted by an entire galaxy of stars, but in a much smaller volume. The basic paradigmatic model of an AGN is a dense gaseous disk through which matter is actively accreting onto a central supermassive black hole. This is surrounded by a region of relatively dense broad-line emitting clouds and then, further out, a region of relatively low-density narrow-line emitting clouds, known as the broad-line region (BLR) and narrow-line region (NLR), respectively. The disk is adding mass to the black hole and, in the process, releasing radiant energy; this region is often referred to as the "central engine". The BLR is relatively near to the central engine, and it is thus a useful probe of this central region. One technique used to explore the BLR is reverberation mapping, which can reveal the structure and kinematics of the emission-line gas. The goal of this project is to explore how a measurement of the black hole mass, using reverberation mapping, within an AGN changes due to systematic effects inherent in using both a wind-based AGN model, as well as combination disk+wind model. This aim is to address two specific questions. First, how does the black hole mass measurement change when we characterize such a region by only two numbers that characterize the velocity dispersion of the emitting gas and the mean reverberation response time? The BLR is a complex region and we seek to determine how much information one loses through a simplified characterization. Second, how does the geometry of the wind affect the measurement of the black hole mass? Specifically, we explored the effects of changing the opening angle of a conical wind and its inclination with respect to an Earth-based observer. These questions are important to help discern the structure of the BLR. This model will help to gather intuition about how the geometry and kinematics of the BLR affect a black hole mass measurement obtained through reverberation mapping.

2 Introduction

2.1 AGN Structure

The structure of an active galactic nucleus (AGN) typically includes the following components (see Figure 1):

- *Central Engine*: A supermassive black hole that is actively accreting and the corresponding dense, gaseous accretion disk. The combination accretion disk-black hole is known as the "central engine."
- *Broad Line Region (BLR)*: A region of relatively dense gas modeled as a region populated with dense line-emitting 'clouds'. This cloud system is usually characterized by some covering factor

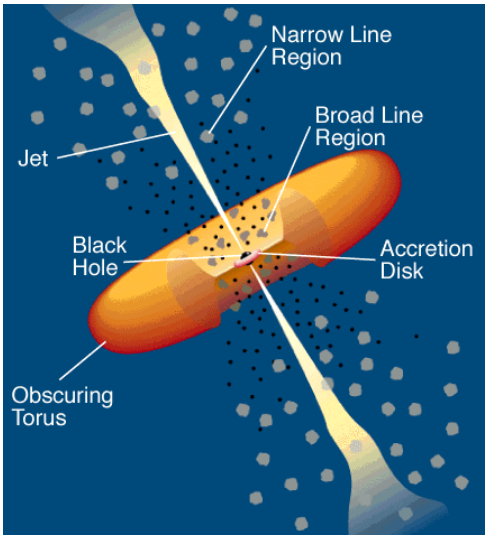

Figure 1: AGN Structure (modified from Urry & Padovani 1995)

(usually ∼10%) that indicates how much of a region of solid angle is occupied by clouds. The broad emission lines are driven by photoionization via the continuum radiation from the central source. This conclusion is supported by observations showing that lines in the BLR vary strongly with the continuum lines; for a change in flux in continuum emission, the BLR lines vary accordingly after the appropriate light travel time. This region is fairly close to the central engine. This proximity can be deduced by the fact that, in general, broad emission lines are produced within a gas in which the atoms and molecules are moving at high velocities. If the emission lines in a region near a black hole are broad, it is likely that the particles are moving at high velocities in the deep gravitational potential around the black hole, and thus that the gas producing these emission lines is near to the black hole. According to Peterson (2001), the BLR can be considered "point-like" because it remains unresolved on the sky even at the 0.01 arcsecond level.

- *Narrow Line Region (NLR)*: A region of relatively less dense gas also modeled by a collection of line-emitting clouds with a smaller filling factor than the BLR. Using a similar argument as for broad emission lines, the NLR is likely to be farther from the black hole than the BLR because the particles in the gas clouds are moving with smaller velocities due to their relatively farther distance from the central supermassive black hole. Additionally, the NLR is resolved on the sky, so it must be larger than the BLR.

- *Obscuring Torus*: A region of dust and gas that obscures our view of the central engine, most likely with a toroidal structure.

- *Relativistic Jet*: A relativistic jet that is observed at radio wavelengths and has a lobe-like structure.

2.2 Emission Lines and Variability

Broad emission lines classically distinguish the ultraviolet through infrared spectra of AGN-based galaxies from their non-AGN counterparts. In fact, the strong emission lines seen in an optical observation of NGC 1068 at Lick Observatory in 1908 is considered the first optical detection of an AGN (Peterson 1997). Figure 2 shows the ultraviolet spectrum for NGC 5548, a Seyfert 1 galaxy, with the broad emission-line features labeled.

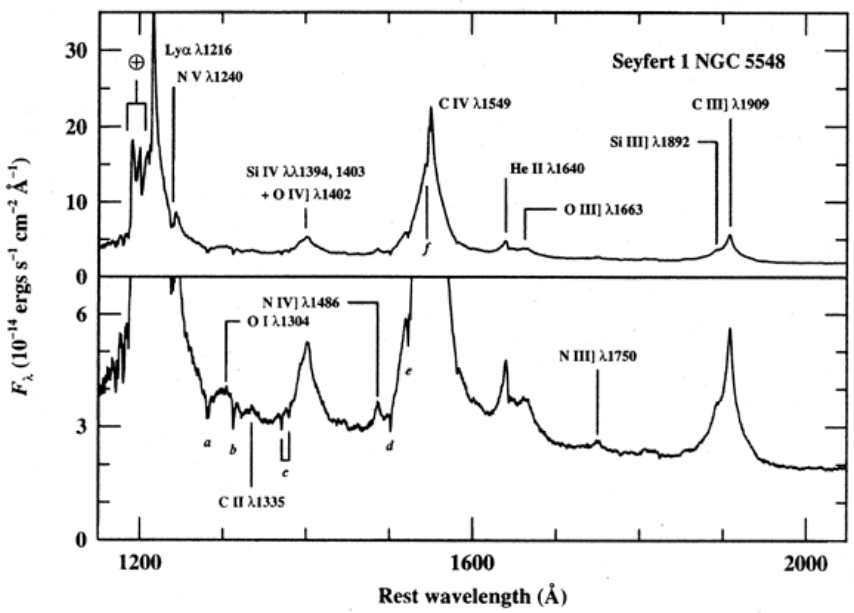

Figure 2: UV spectrum of NGC 5548 with broad emission lines highlighted (from Peterson 1997)

An important aspect of AGN observations is the fact that the spectral lines vary with time; this quality is known as variability. Specifically, the two variations that are important to this study are variations in the UV/optical continuum and variations in the broad emission lines. AGNs appear to vary aperiodically and with variable flux at all wavelengths at which they have been observed. Rapid variability in the continuum of greater than about 0.01 magnitudes on time scales as short as days imply a small size for the continuum emitting region based on causality arguments. The variations must be on the order of the light-travel time across the emitting region if this region is causally connected; the region must be causally connected because the variations would be averaged out if they were chiefly stochastic in nature and the number of sources of these random variations was large. Note that the source of continuum emission is not well understood, but it seems likely that it arises from instabilities in the accretion disk (Peterson 1997).

Variability in the broad emission lines is pronounced on scales of months to years, but is subtler on shorter time scales. The emission-line variations relative to continuum variations can be used to explore

the kinematics and other details of AGN structure on small scales, perhaps as small as microarcseconds, and the kinematics and geometry of the BLR can also be constrained using the emission-line response relative to continuum variations. The delay between the original continuum variations and the response of the emission lines can be used to infer the size of the BLR. Observations of the response of Hβ lines to continuum variations in Arakelian (Akn) 120 implied, for example, a BLR size of less than 1 light-month. If we assume that the continuum variations originate from a single, point-like source, then for a supermassive black hole of approximately $10^7 - 10^8 M_\odot$, the corresponding BLR size would be on the order of a few light-days (Peterson 2001). Finally, because broad emission lines tend to vary with the UV/optical continuum on small time scales on the order of days, one can conclude that the BLR clouds are close to the continuum source and thus that the size of the BLR is small. Furthermore, the line-emitting clouds must be optically thick. If the clouds were optically thin, then we would not observe a significant response in the BLR to continuum variations.

3 Reverberation Mapping

3.1 Basic Theory

One technique used to explore the BLR is reverberation mapping, which can reveal the structure and kinematics of the emission-line gas. When some radiative event happens in the continuum near the central engine, these photons will stream outward toward the BLR. Some of these photons will interact with BLR clouds, depending on the covering factor, and some of the photons that interact with the BLR will then travel toward the observer.

For example, consider the situation below in Figure 3, in which the BLR is modeled as a thin shell around the central source. Viewed in cross-section, the BLR will appear as a ring around the central

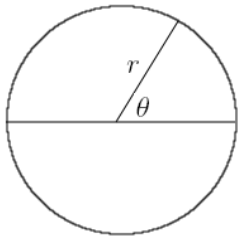

Figure 3: BLR cross-section, with a cloud at angle θ and distance r from the central source (modified from Peterson 1997)

source. When some radiative event happens in the continuum, the photons involved will propagate radially outward in all directions toward the BLR. If the covering factor of the BLR is the typical value mentioned earlier, then around 10% of the photons emitted originally will interact with clouds in the

BLR. These photons will be reprocessed into emission-line photons and then travel radially away from the cloud in all directions. Some of these reprocessed photons will therefore travel toward an Earth-based observer.

When these original photons interact with the BLR, this flash of light will appear in the emission lines. The time delay between the original event (seen in the continuum lines) and the response in the BLR emission lines is equal to the light travel time between the source and the cloud along the ring. The observer will see the same time delay, τ, for all clouds that lie on surfaces of constant time delay, known as isodelay surfaces. This surface is an ellipsoid with the source and the observer at the foci. However, because the observer is effectively located infinitely far away from the source, the isodelay surfaces can be modeled as paraboloids. If we take a cross-section of the BLR and several isodelay surfaces, the result is a ring intersected by several parabolas, as shown in Figure 4. The time delay, τ, between the original

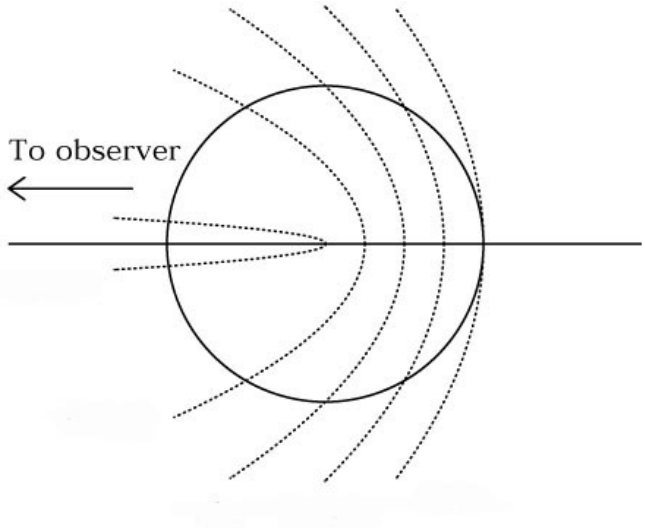

Figure 4: Cross-section of BLR with isodelay surfaces (modified from Peterson 2001)

event and the response in the BLR emission lines for this situation is given by the equation for a parabola in polar coordinates

$$\tau = \frac{r}{c}(1 + \cos\theta). \tag{1}$$

Thus, for each ring of clouds, the parabolic isodelay surface intersects the BLR at two points (Peterson 1997).

When we sum over the contribution from each isodelay surface, we obtain a one-dimensional transfer function, which represents the response of the BLR with respect to time delay. At each delay, the total response is the sum over the response measured at each point along the intersection of the BLR with a particular isodelay surface. Thus, each point on the one-dimensional transfer function is the sum over

the responses at each intersection of the BLR with the isodelay surface corresponding to that time delay, and the entire function traced out shows how these sums change with time delay. In other words, the function shows how the response changes at each isodelay surface. The strength of the response at a specific time delay is between 0 and 1, where 0 is no response and 1 represents a complete response to the original continuum photon with an emission-line photon. line. An example 1D transfer function is shown below, in Figure 5.

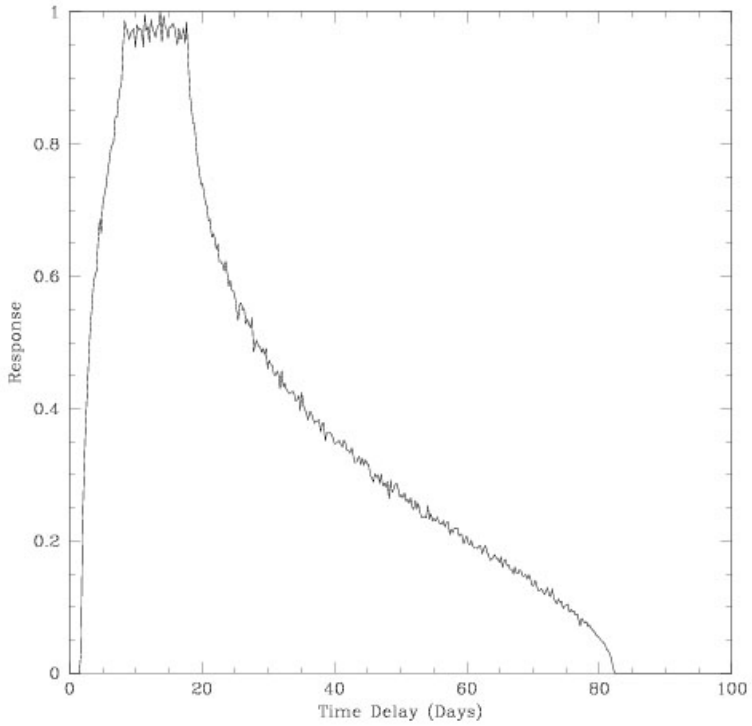

Figure 5: 1D transfer function for a BLR with a Keplerian disk structure at $i = 40°$ and $\alpha = 0.0$

Next, using Doppler shifts in the BLR emission-line profile, the line-of-sight velocity of the clouds can be measured. For each photon that interacts with a cloud, its emission-line photon will be Doppler shifted with respect to the rest wavelength of the line in consideration. Two emission-line photons, one blue-shifted and one red-shifted, along an isodelay surface will (as expected) have the same time delay. This can be shown in a plot of time delay versus line-of sight velocity, as shown in Figure 6.

The strength of the response at a specific measured velocity versus line-of-sight velocity, in km/s, can be plotted. The response varies between 0 and 1 as with the one-dimensional transfer function. This function is the velocity profile of the BLR clouds in the shell. An example velocity profile is shown below in Figure 7

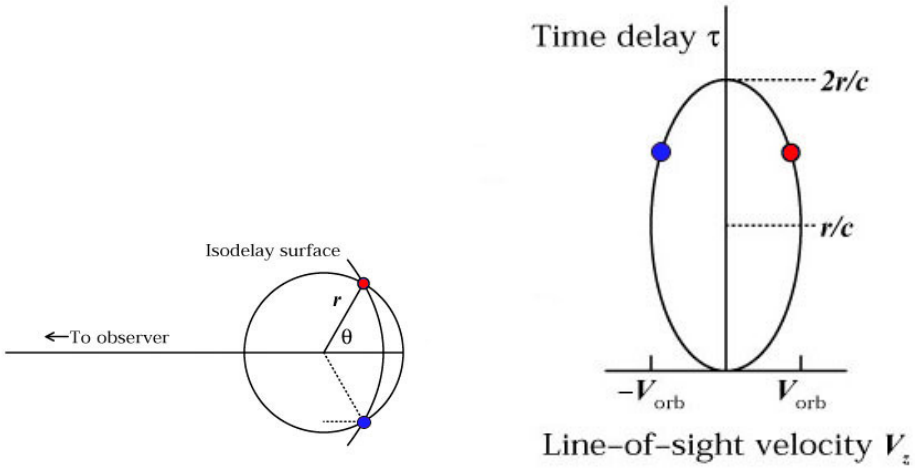

(a) Two clouds on an isodelay surface on a ring-shaped BLR cross-section. One cloud is moving toward the observer (blue-shifted, marked with a blue dot) and the other is moving away from the observer (red-shifted, marked with a red dot).

(b) The same two clouds plotted in $v - \tau$ space. They will have the same time delay, since they are on the same isodelay surface, but the red-shifted cloud will have a positive velocity, and the blue-shifted cloud will have a negative velocity. If dots were placed on this plot for all isodelay surfaces that intersect the BLR cross-section, they would trace out an ellipse with a major axis equal to the light-travel time across the BLR.

Figure 6: Two different representations of two clouds, one red-shifted and one blue-shifted, that lie along the same isodelay surfaces. In 6(a), the clouds are shown in r, θ space; in 6(b), the clouds are shown in v, τ space (modified from Peterson 2001).

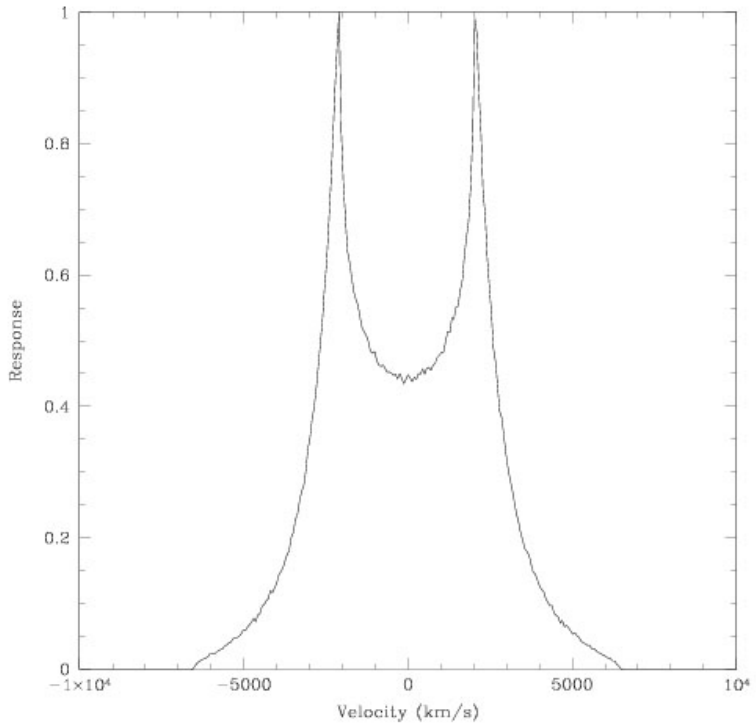

Figure 7: Velocity profile for a BLR with a Keplerian disk structure at $i = 40°$ and $\alpha = 0.0$

3.2 Using Reverberation Mapping to Find the Black Hole Mass

The velocity of a particle around a black hole can be expressed using the familiar form for circular velocity in a gravitational potential

$$v^2 = \frac{GM}{r} \Longrightarrow M = \frac{rv^2}{G}. \tag{2}$$

For a system of particles, we use a similar formula, where r is some representative size of the system, σ is some representative velocity dispersion, and a dimensionless factor f subsumes information about the details of the BLR structure, kinematics and orientation,

$$M = \frac{fr\sigma^2}{G}. \tag{3}$$

Note that $r = c\tau$, where τ is the light-travel time between the source and the BLR. Thus, this equation becomes

$$M = \frac{fc\tau\sigma^2}{G}. \tag{4}$$

The value τ in equation 4 is given by the centroid of the one-dimensional transfer function. We characterize the motion of the clouds along the line of sight by the Full Width at Half Maximum (FWHM) of the velocity profile, and will be denoted Δv. Thus, the mass of the central black hole of an AGN, using a one-dimensional transfer function and a velocity profile, measured observationally or modeled theoretically, is given by

$$M = \frac{fc\tau(\Delta v)^2}{G}. \tag{5}$$

4 Modeling a Simple Outflow

We started by modeling a spherical outflow using two simple radial velocity distributions. The wind geometry is conical, in which ω is the semi-opening angle of the cone, as indicated in Figure 8. We first modeled a radial ballistic outflow, with

$$\frac{v(r)}{r} = \frac{v_{\min}}{r_{\min}}$$

$$v(r) = \left(\frac{v_{\min}}{r_{\min}}\right) r = \left(\frac{v_0}{r_{\min}}\right), \tag{6}$$

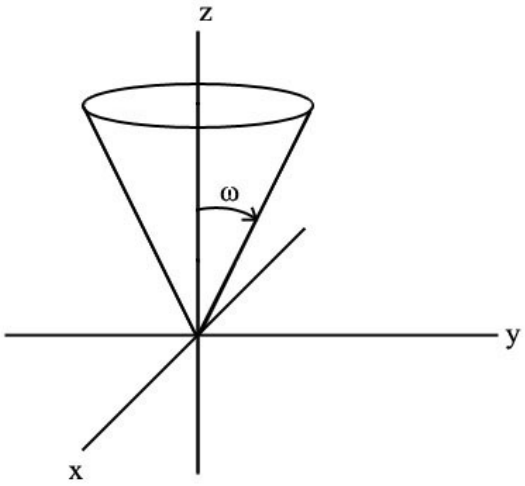

Figure 8: Schematic of conical outflow with opening angle ω labeled

where $r_{\min}$ is the inner radius of the wind, with respect to the black hole, and $v_{\min} = v_0$ is the "startup velocity" of the wind (i.e., the velocity at r_{min}). We also modeled an outflow at escape velocity, with

$$v(r) = \sqrt{\frac{GM_\bullet}{r}}, \tag{7}$$

where $G = 6.67 \times 10^{-11} Nm^2 kg^{-2}$ and $M_\bullet$ is the black hole mass. Note that in our test case we actually used a spherical *inflow*, because the results we were checking against modeled an inflow at escape velocity (free fall). This is only a difference in sign, and it is trivial to modify this for an outflow.

For the ballistic model, an initial velocity must be defined (i.e., we must "start" the wind); for the outflow at escape velocity, the initial velocity is determined by the inner radius of the outflow and the black hole mass. Then, the position and velocity of each cloud is transformed from the frame of the AGN to the frame of an Earth-based observer. For a calculation of this transformation, see Appendix A. For both cases, the program took in a number of inputs and output a one-dimensional transfer function, a radial velocity profile, and a two-dimensional velocity delay map. The 2D velocity delay map, as shown in Figure 9, measures the response of the BLR as a function of *both* the radial velocity and the time delay. The change in response is measured with color: darker areas indicate a higher response and lighter areas indicate lower response. The only difference between the two, in terms of inputs, is that the ballistic program takes in an initial velocity and the outflow at escape velocity takes in a black hole mass with no explicitly defined initial velocity. The inputs for the simple models include:

- Minimum wind radius, r_{min}, in units of light-days (ld)

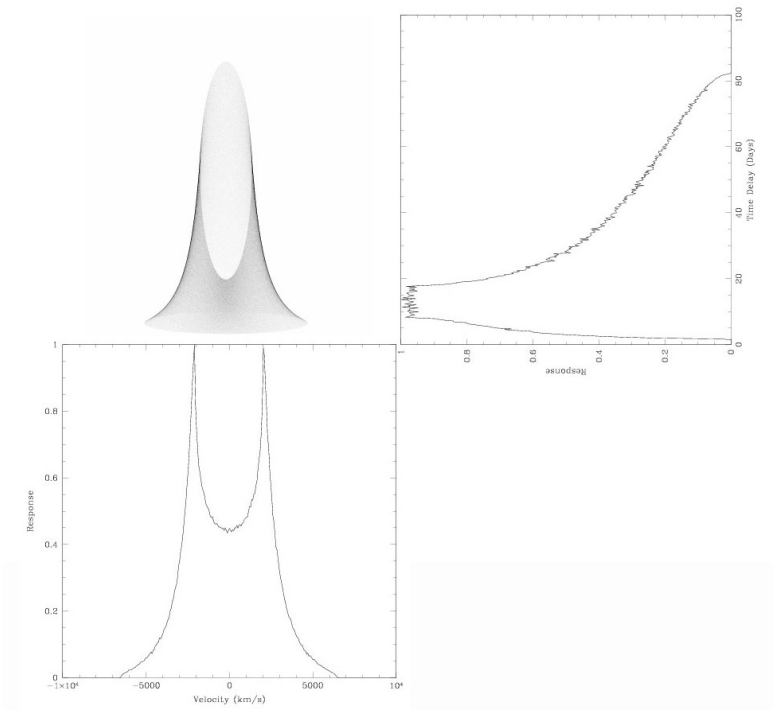

Figure 9: 2D velocity delay map with corresponding 1D transfer function and velocity profile for a BLR with a Keplerian disk structure at $i = 40°$ and $\alpha = 0.0$

- Maximum wind radius, r_{max}, in units of light-days (ld)
- Inner opening angle, ω_{min}, in units of degrees
- Outer opening angle, ω_{max}, in units of degrees
- Black hole mass, $M_\bullet$, in units of solar masses, $M_\odot$, for outflow at escape velocity
- Initial velocity, v_0, in units of km/s, for the ballistic outflow
- Inclination of the AGN system with respect to an Earth-based observer, i, in units of degrees. Note that $i = 0°$ corresponds to a face-on AGN, and $i = 90°$ corresponds to edge-on.
- Emission-line asymmetry parameter, A, defined within the relation for cloud emissivity toward the observer,

$$\epsilon(\theta) = \frac{1 + A\cos\theta}{2}, \tag{8}$$

where θ is the angle between the line-of-sight and the cloud. If $A = 0$, then the emissivity is a constant (i.e., the line emission is isotropic). If $A = 1$, then the emissivity behaves similar to lunar phases. In other words, $\epsilon = 1$ at $\theta = 0°$, and $\epsilon = 0$ at $\theta = 180°$. The lines we observe will be influenced by the emissivity of the clouds and thus the line asymmetry parameter, A.

- Radial response index, α, which is unitless and indicates how the BLR clouds should respond as r increases. The radial response goes as r^{α}. So, $\alpha = 0$ corresponds to uniform response from all clouds in the BLR, regardless of r. But if $\alpha = -2.0$, for example, the response in the BLR drops off like $1/r^2$.
- Number of steps in ω, which effectively defines the step size from ω_{min} to ω_{max}.
- Number of steps in r, which steps outward away from the black hole along lines of constant ω from r_{min} to r_{max}

Note that the number of steps in ω and r effectively determine the number of clouds in the system. So, keeping the number of tries in ω and in r constant means that we place the same number of clouds into the system every time. We compared our results with those of Welsh & Horne (1991) to test the model. Thus, we used the same physical parameters for r_{min}, r_{max}, $M_{\bullet}$, and v_0, as appropriate: $r_{min} = 5$ ld, $r_{max} = 50$ ld, $M_{\bullet} = 10^8\ M_{\odot}$, and $v_0 = 1000$ km/s. Also, we tested our model in the case of a spherical wind, which can be solved analytically. For the spherical test case, we defined $0° \leq \omega \leq 180°$, with a step size between $0.001° \leq \omega \leq 0.01°$.

5 Monte Carlo Simulations of the Outflow

Next, we transformed the model from one which stepped through ω and r to one which utilized Monte Carlo methods. We started with a uniform random number distribution in the range [0,1]. Due to the nature of the projection of the outflow onto the sky, the random number distribution was weighted such that it is proportional to $\sin(\omega)$, as shown in Figure 10. We placed clouds randomly throughout a cone

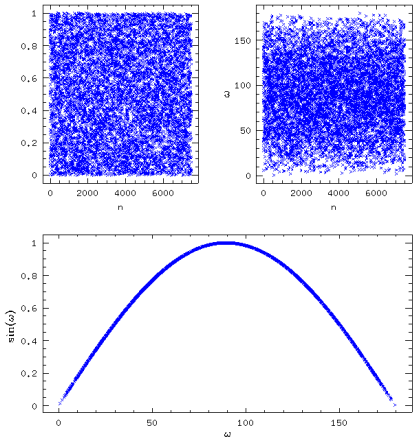

Figure 10: Uniform and weighted random number distributions used for the Monte Carlo model

between $[\omega_{min}, \omega_{max}]$. We then compared the results of this Monte Carlo model to the results from Welsh & Horne (1991). Figures 11 and 12 show our results.

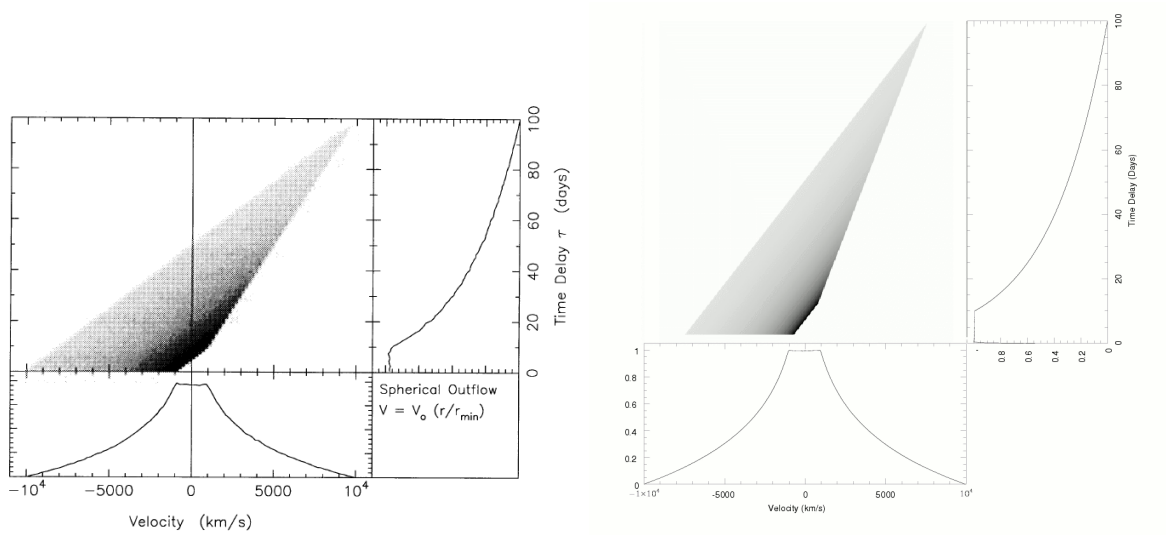

(a) Spherical Ballistic Outflow from Welsh & Horne 1991 (b) Ballistic Outflow using the Monte Carlo Model, Spherical Test Case

Figure 11: Comparison of our results with Welsh & Horne 1991 for a spherical ballistic outflow

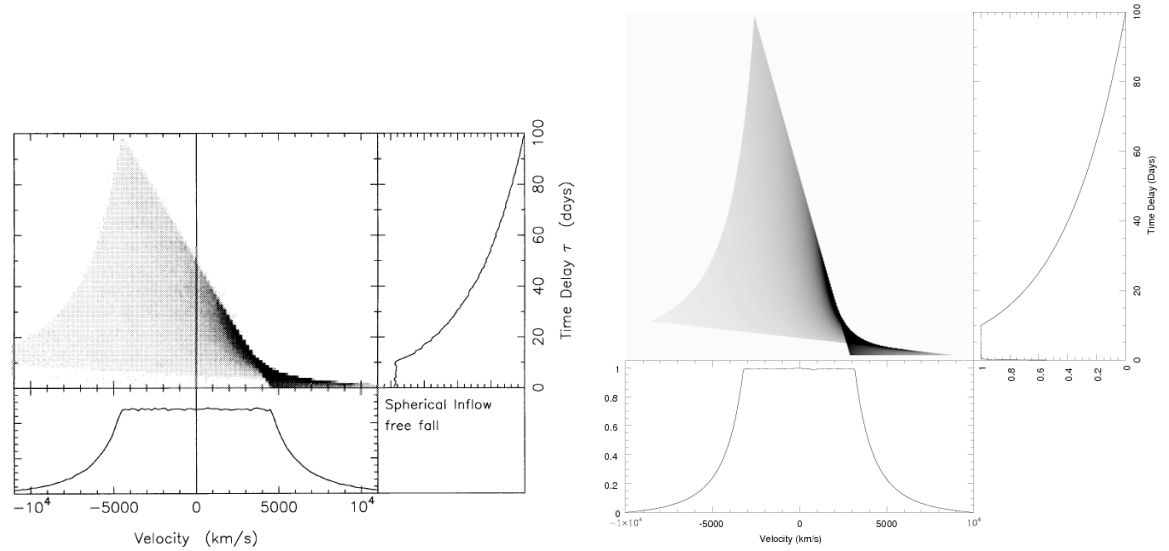

(a) Spherical Inflow at Escape Velocity from Welsh & Horne 1991 (b) Inflow at Escape Velocity using the Monte Carlo Model, Spherical Test Case

Figure 12: Comparison of our results with Welsh & Horne 1991 for a spherical inflow at escape velocity

6 Examination of Systematic Effects

Equation 5 can be manipulated to give a value for the scaling factor,

$$f = \frac{GM_\bullet}{c\tau(\Delta v)^2}. \tag{9}$$

This value can give us an idea about how a wind-based BLR would affect our measurement of the black hole mass, $M_\bullet$. I chose to examine two specific cases for this paper: a jet-like geometry ($0° \leq \omega \leq 15°$) and a disk wind-like geometry ($75° \leq \omega \leq 90°$).

We expect f to be on the order of 1, and thus that the geometrical aspects of the BLR would only scale the black hole mass measurement by a few. There are two major reasons for this estimate of f. First, the $M - \sigma_\star$ relation, where $\sigma_\star$ is the velocity dispersion of stars in the host galaxy, is another way to measure black hole mass. If the black hole mass obtained using the $M - \sigma_\star$ relation is compared to the result from reverberation mapping, the value of f is constrained to be less than 10. Second, the quasar luminosity defines a minimum mass for the black hole, the Eddington mass. The measured black hole mass must be at least as large as the Eddington mass. If the value of f is large, then the measured mass is heavily underestimated, considering this additional criterion.

First, look at the jet-like model. Figure 13 shows this geometry schematically, and Figure 14 is a plot of f versus inclination (in degrees) for five different values of α. It is immediately obvious that the

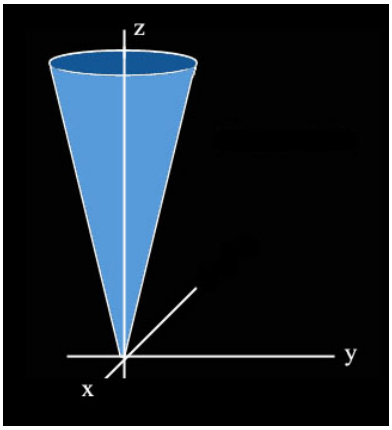

Figure 13: Jet-like wind geometry, $0° \leq \omega \leq 15°$

value of f disagrees with the expected value by several orders of magnitude. This discrepancy is most pronounced as inclination approaches face-on and as radial response approaches a constant. The best agreement comes between $40° \leq i \leq 80°$, but even this is about one order of magnitude too large. This makes sense because, if we were to observe this wind, all of the clouds would be concentrated into a narrow cone, and the line-of-sight velocity dispersion will be very small, which in turn leads to a gross

underestimation of the mass.

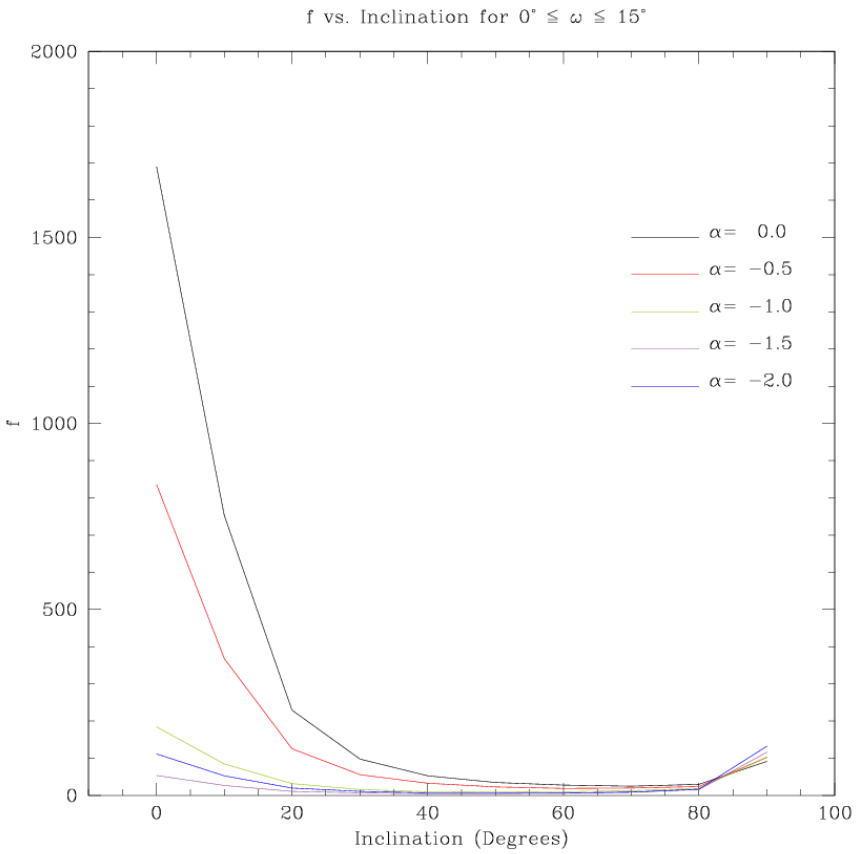

Figure 14: f vs. i for $0° \leq \omega \leq 15°$

Next, Figure 15 shows, schematically, a disk wind-like geometry, and Figure 16 shows f vs. i for this model, again for five different values of α. As with the jet-like geometry, the value of f is too large

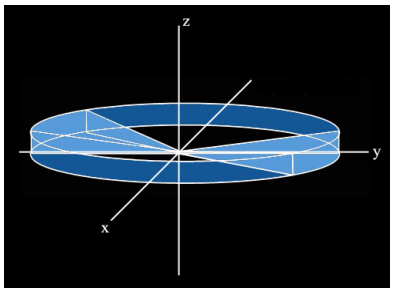

Figure 15: Disk wind-like geometry, $75° \leq \omega \leq 90°$

by at least an order of magnitude, especially at low inclinations and radial response values with little to no dependence on r. At inclinations between $20° \leq i \leq 90°$, the value of f is reasonable, unlike in the jet-like geometry, and this makes sense intuitively. If one were to observe this wind at $i = 0°$, it is highly unlikely that a satisfactory observation could be made, because it would be extremely difficult to make radial velocity measurements using Doppler shifts in this case. However, with higher inclination,

we would be able to see more of the wind and observe a wider range of line-of-sight velocities.

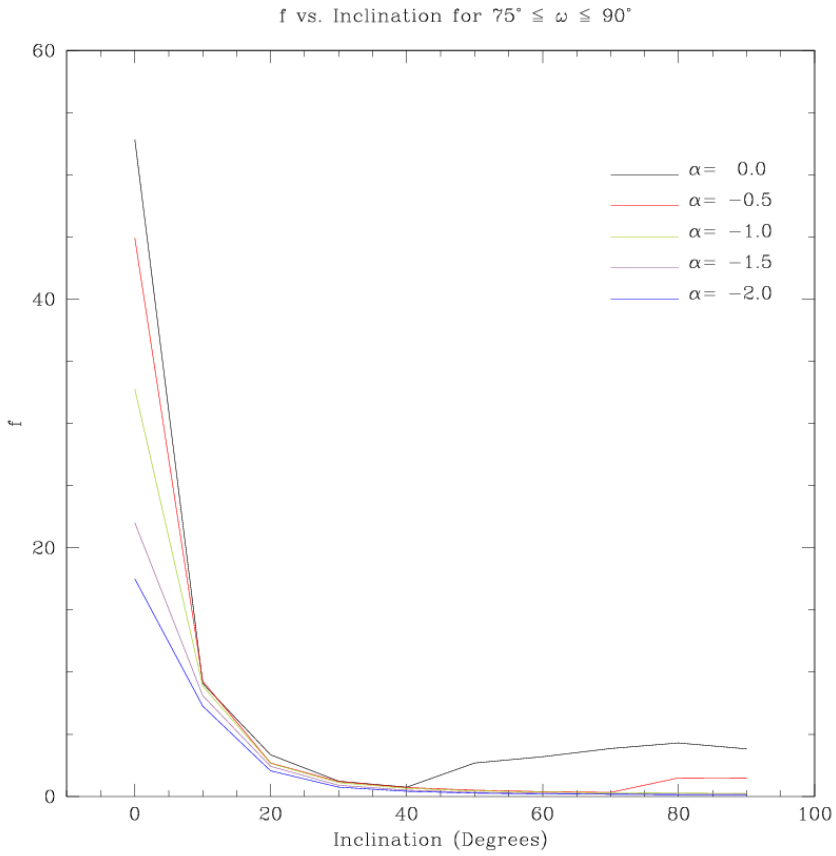

Figure 16: f vs. i for $75° \leq \omega \leq 90°$

7 Caveats For The Model and Future Work

This model should be considered a "toy model", and thus should be used for primarily intuition-gaining purposes. There is no real physics included in this model. A more accurate model would include an emissivity law as a function of r. Additionally, the cloud parameters, such as the density and radius, must be considered. Third, the dynamics of the wind are not considered (i.e., we did not specify what is driving the wind).

Overall, both of the geometries represented here produce results that are not consistent with expectations. Thus, if we are to continue consideration of a wind-based BLR model with a radial velocity field, then these two extreme geometries could be excluded on the basis that they are physically absurd. Cases including intermediate opening angle ranges (i.e., between $15° \leq i \leq 75°$ and opening angle ranges in larger "chunks" than just 15° should be considered in further exploration of this model. Additionally, we are currently improving the resolution of the model in α (i.e., we are simulating the system in steps

of $\alpha = 0.1$ rather than $\alpha = 0.5$.) Future work involving this model will examine, as earlier stated, more intermediate opening angle ranges. Additionally, a disk component will be added to the model to form a disk+wind BLR geometry, and this combination will be considered.

Appendix A: Transformation to the Observer's Frame

Start with a cone in the frame of the AGN system, (x, y, z), shown in Figure 17.

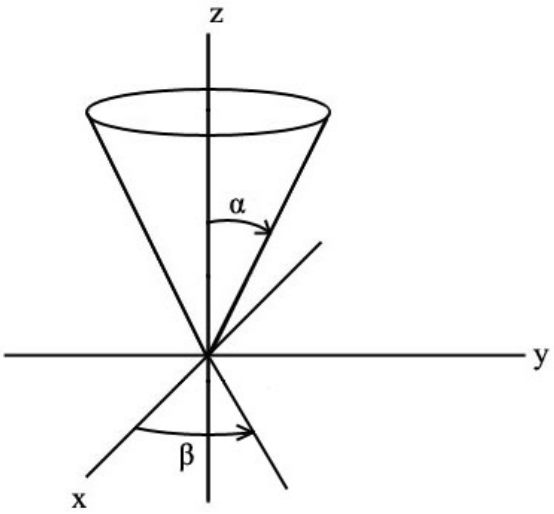

Figure 17: A cone in the AGN system frame. α is the polar angle, and β is the azimuthal angle.

$$\vec{x} = \begin{pmatrix} x \\ y \\ z \end{pmatrix} = \begin{pmatrix} r\sin\alpha\cos\beta \\ r\sin\alpha\sin\beta \\ r\cos\alpha \end{pmatrix}. \tag{10}$$

Next, rotate the cone by angle ϕ about the z axis into a (ξ, η, ρ) system, as shown below in Figure 18.

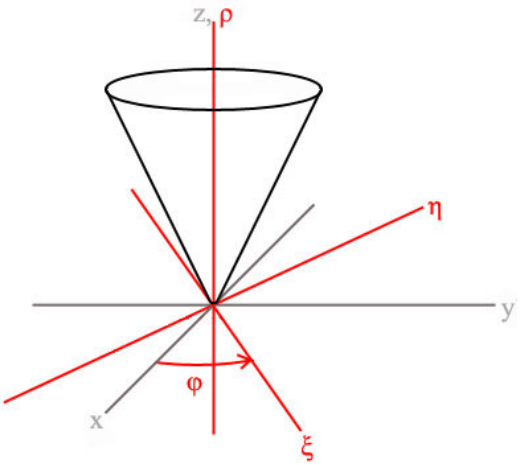

Figure 18: Rotation by ϕ about z from $(x, y, z) \rightarrow (\xi, \eta, \rho)$

$$\vec{\xi} = R(\phi)\vec{x} \tag{11}$$

where

$$R(\phi) = \begin{pmatrix} \cos\phi & \sin\phi & 0 \\ -\sin\phi & \cos\phi & 0 \\ 0 & 0 & 1 \end{pmatrix}. \tag{12}$$

Then, rotate the cone by angle θ about the ρ axis into a (ξ', η', ρ') system, shown below in Figure 19.

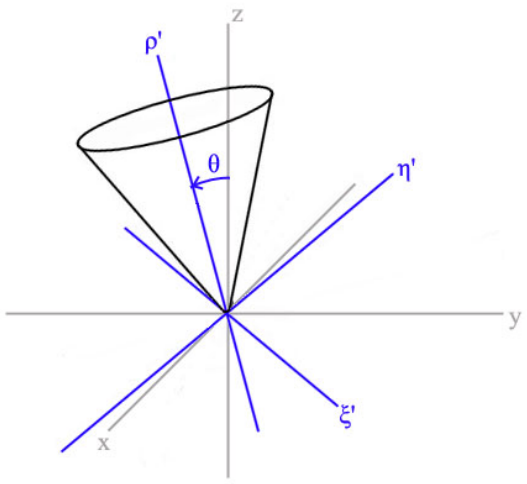

Figure 19: Rotation by θ about ξ from $(\xi, \eta, \rho) \rightarrow (\xi', \eta', \rho')$

$$\vec{\xi'} = R(\theta)\vec{\xi} \tag{13}$$

where

$$R(\theta) = \begin{pmatrix} 1 & 0 & 0 \\ 0 & \cos\theta & \sin\theta \\ 0 & -\sin\theta & \cos\theta \end{pmatrix}. \tag{14}$$

Finally, rotate the cone by angle ψ about the ρ' axis into the (x', y', z') system, which is the observer's frame, as shown in Figure 20.

$$\vec{x'} = R(\psi)\vec{\xi'} \tag{15}$$

where

$$R(\psi) = \begin{pmatrix} \cos\psi & \sin\psi & 0 \\ -\sin\psi & \cos\psi & 0 \\ 0 & 0 & 1 \end{pmatrix}. \tag{16}$$

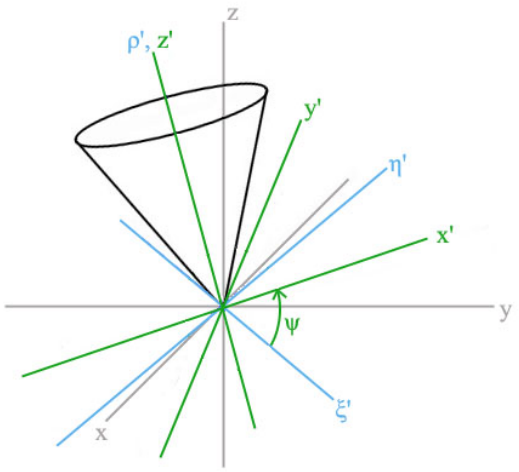

Figure 20: Rotation by ψ about ρ' from $(\xi', \eta', \rho') \rightarrow (x', y', z')$, which is the observer's frame

So, the transformation from the AGN frame ($\vec{x}$) to the observer's frame ($\vec{x'}$ is the following

$$\vec{x'} = R(\psi)\vec{\xi'} = R(\psi)R(\theta)\vec{\xi} = R(\psi)R(\theta)R(\phi)\vec{x} = A\vec{x} \tag{17}$$

where the total rotation matrix is then

$$A = R(\psi)R(\theta)R(\phi)$$

$$= \begin{pmatrix} \cos\psi\cos\phi - \sin\psi\sin\phi\cos\theta & \cos\psi\sin\phi + \sin\psi\cos\phi\cos\theta & \sin\psi\sin\theta \\ -\sin\psi\cos\phi - \cos\psi\sin\phi\cos\theta & -\sin\psi\sin\phi + \cos\psi\cos\phi\cos\theta & \cos\psi\sin\theta \\ \sin\phi\sin\theta & -\cos\phi\sin\theta & \cos\theta \end{pmatrix}. \tag{18}$$

Now, the angle that really matters here is θ, which is the inclination of the system. I will rename this variable i, such that $\cos\theta = \cos i$ and $\sin\theta = \sin i$. The system is symmetric in ϕ and ψ, so we can define them arbitrarily. It is convenient so say that $\phi = \psi = 0$, such that $\cos\phi = \cos\psi = 1$ and $\sin\phi = \sin\psi = 0$. This transforms A into

$$A = \begin{pmatrix} 1 & 0 & 0 \\ 0 & \cos i & \sin i \\ 0 & -\sin i & \cos i \end{pmatrix}. \tag{19}$$

Thus,

$$\begin{pmatrix} x' \\ y' \\ z' \end{pmatrix} = \begin{pmatrix} 1 & 0 & 0 \\ 0 & \cos i & \sin i \\ 0 & -\sin i & \cos i \end{pmatrix} \begin{pmatrix} x \\ y \\ z \end{pmatrix}. \tag{20}$$

This implies, therefore, that

$$x' = x = r \sin\alpha \cos\beta, \tag{21}$$

$$y' = (\cos i)y + (\sin i)z = r(\cos i \sin\alpha \sin\beta + \sin i \cos\alpha), \tag{22}$$

and

$$z' = (-\sin i)y + (\cos i)z = -r(\sin i \sin\alpha \sin\beta - \cos i \cos\beta). \tag{23}$$

References

[1] Peterson, B.M. 1997, An Introduction to Active Galactic Nuclei (Cambridge: Cambridge University Press).

[2] Peterson, B.M. 2001, in The Starburst-AGN Connection, ed., I. Aretxaga, D. Kunth, R. Mujica (Singapore: World Scientific), p. 3

[3] Urry, C.M & Padovani, P., PASP, 107, 803

[4] Welsh, W.F. & Horne, K. 1991, ApJ, 379, 586